



# Effect of cooling rate on microstructure and microhardness of hypereutectic Al–Ni alloy

A. P. Carrara<sup>1</sup> · R. Kakitani<sup>1</sup> · A. Garcia<sup>1</sup> · N. Cheung<sup>1</sup>

Received: 3 August 2020 / Revised: 27 October 2020 / Accepted: 4 December 2020 / Published online: 12 January 2021  
© Wrocław University of Science and Technology 2021

## Abstract

High solidification cooling rates during unsteady-state conditions of solidification of Al-based alloys can induce different microstructural length scales or metastable phases, leading to improved properties. The present study aims to characterize the microstructural arrangement of the hypereutectic Al–8 wt%Ni alloy, unidirectionally solidified in unsteady-state heat flow conditions, examining the influence of the cooling rate in the development of the Al–Al<sub>3</sub>Ni eutectic and the primary phase. A columnar-to-equiaxed macrostructural transition is shown to occur at a solidification cooling rate ( $\dot{T}$ ) of about 4.8 °C/s, with different microstructures associated with each morphological zone. The observation of microstructures of hypoeutectic, eutectic and hypereutectic Al–Ni alloys, has permitted an asymmetric coupled zone diagram to be proposed. The microstructural interphase spacings of the Al–8 wt%Ni alloy are experimentally determined and correlated to  $\dot{T}$ , and the Vickers microhardness (HV) is shown to decrease with the increase in such spacings. The higher experimental HV profile of the examined hypereutectic alloy as compared to that of the eutectic Al–Ni alloy is attributed to the formation of a supersaturated solid solution of Ni in  $\alpha$ -Al.

**Keywords** Al–Ni alloys · Solidification · Columnar-to-equiaxed transition · Microstructure · Microhardness · Coupled zone diagram

## 1 Introduction

Alloys of the Al–Ni system are receiving significant attention due to the microstructural arrangement combining the light  $\alpha$ -Al matrix and the intermetallics (IMC), responsible for excellent mechanical properties until 500 °C and good corrosion resistance [1, 2], fulfilling, in this regard, the requirements of aerospace and transportation industries. In the Al-rich part of the Al–Ni phase diagram, the Al–Al<sub>3</sub>Ni eutectic is expected to occur with a fiber morphology, and according to the literature, both the fluidity and the hot tearing resistance increase with the increase in the eutectic fraction [3–5]. With a view to sustaining these characteristics and improve mechanical properties, third elements [6–8] have been usually added to form solid solutions with  $\alpha$ -Al and precipitate new intermetallics in the eutectic. However,

studies examining the effects of microstructural features on the mechanical properties are restricted to hypoeutectic Al–Ni compositions, with few ones concerning hypereutectic alloys.

Hypereutectic alloys are considered as in situ metal-matrix composites (MMC), where the microstructure is formed by the primary phase, usually an intermetallic compound, surrounded by the eutectic matrix, and these alloys are demanded for wear resistance and high temperature applications. In the case of hypereutectic Al–Ni alloys, a great amount of  $\alpha$ -Al + Al<sub>3</sub>Ni is formed around the primary Al<sub>3</sub>Ni, whose orientation can be controlled through high magnetic fields [9], aligning the Al<sub>3</sub>Ni fibers and designing a better reinforcement.

Besides magnetic manipulation, at high solidification cooling rates ( $\dot{T}$ ), or unsteady-state conditions of solidification, typical microstructures or metastable phases may develop, leading to improved properties. At high  $\dot{T}$  and low thermal gradient, the halos in primary Si of hypereutectic Al–Si alloys grew as dendrites, promoting increase in the ultimate tensile strength and elongation [10]. Gonzalez et al. [2] found the metastable Al<sub>9</sub>Ni<sub>2</sub> phase after melt

✉ N. Cheung  
cheung@fem.unicamp.br

<sup>1</sup> Department of Manufacturing and Materials Engineering,  
University of Campinas - UNICAMP, Campinas,  
SP 13083-860, Brazil

spinning of the hypereutectic Al–8.3 wt%Ni alloy, and the increment of the process speed (i.e. increase in  $\dot{T}$ ) allowed a higher fraction of  $\text{Al}_3\text{Ni}_2$  to be formed. In benefit, the replacement of  $\text{Al}_3\text{Ni}$  with  $\text{Al}_3\text{Ni}_2$  increased the Vickers microhardness by more than 150%. Using quite different cooling conditions during solidification of a hypereutectic Al–2.5 wt%Mn–0.5 wt%Cr alloy, Feng et al. [11] reported a microstructure transition from a dendritic morphology in furnace cooling to fully eutectic in iron mold cooling, i.e., using a mold with higher thermal conductivity, the cooling rate increased leading to a refined microstructure and better mechanical properties.

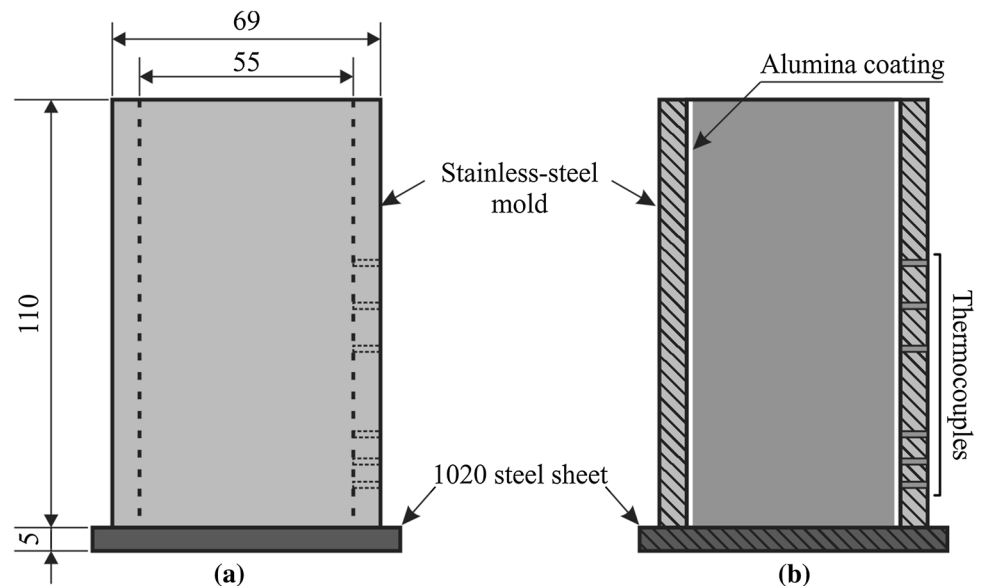
For hypereutectic Al–12.4 wt%Mg–9.5 wt%Si [12] and Al–20 wt%Si–(0.7 wt%Cr) [13] alloys, aside from microstructural refinement, high cooling rates were reported to induce morphological changes and increase in the amount of primary phases per area. The authors observed that the  $\text{Mg}_2\text{Si}$  IMC presented an irregular polyhedral morphology at 1 °C/s; however, as the cooling rate increased, the IMC assumed a regular shape and finally evolved to dendrites at 39 °C/s. In the case of the Al–Si–(Cr) alloy, Si was the primary phase, having a large star-like morphology for low cooling rates and either compact plate-like or octahedral morphologies for high cooling rates. Since hypereutectic alloys are usually brittle, smaller IMCs and higher density per area mean a better distribution of the phases, which can lead to improvements in both ultimate tensile strength ( $\sigma_U$ ) and elongation ( $\delta$ ). In this sense, Kakitani et al. [14] and Dias et al. [15] added 1.5 wt%Mg and 3.2 wt%Bi, respectively, into an Al–15 wt%Si alloy directionally solidified under unsteady-state conditions, and reported that the highest  $\sigma_U$  and  $\delta$  were achieved for  $\dot{T} > 18$  °C/s. For low cooling rates,  $\sigma_U$  was shown to be up to 30% lower and  $\delta$  could decrease more than 25%.

Therefore, the aim of this study is to characterize the microstructural arrangement of the hypereutectic Al–8 wt%Ni alloy, unidirectionally solidified in unsteady-state conditions, examining the influence of the cooling rate in the development of the Al– $\text{Al}_3\text{Ni}$  eutectic and the primary phase. After establishing correlations between representative microstructural spacings and the cooling rate, Vickers microhardness will be evaluated against different types and length scale of the microstructure.

## 2 Experimental procedure

An Al–8 wt%Ni alloy was prepared using commercial grade Al (99.85 wt% Al, 0.07 wt% Fe, 0.05 wt%Si and 0.03% of others) and Ni (99.97 wt%Ni, 0.004% Fe and 0.025% of others). The commercial grade Al was placed in a SiC crucible and melted in an electric resistance furnace at 850 °C for 1 h, followed by the addition and homogenization of Ni. The crucible returned to the furnace for 0.5 h, to ensure total diffusion of Ni, and then, the molten alloy was poured into a cylindrical stainless-steel mold having an inner diameter of 55 mm and a height of 110 mm, as shown in Fig. 1. The inner wall of the mold was coated with alumina and the surface of the bottom part of mold (a SAE 1020 steel sheet) was ground and polished using SiC papers up to a 1200 grit finish. Six fine type K thermocouples were placed along the length of the mold, capable to monitor and acquire the temperature before and during solidification at a frequency of 5 Hz. The mold was placed in a unidirectional solidification apparatus, with controllable temperature through radial electrical wiring. The alloy was remelted, and once the liquid metal reached 10% above the *liquidus* temperature ( $T_L = 672$  °C), the electrical winding was disconnected, and

**Fig. 1** a Front view and b section view of the mold. All dimensions in mm



the bottom of the mold was cooled by water.  $\dot{T}$  was calculated by the time-derivative of the cooling curves furnished by the thermocouples just after the passage of the eutectic isotherm by each thermocouple. Figure 2 presents the partial Al–Ni phase diagram calculated by the Thermo-Calc software, using the TCBIN database, and highlighting in green the studied alloy composition. Under equilibrium conditions of solidification, which is not the case of the present investigation, it can be observed at the phase diagram, that the expected phases are  $\text{Al}_3\text{Ni}$  as primary phase and a eutectic mixture of  $\alpha\text{-Al}$  and  $\text{Al}_3\text{Ni}$ .

Longitudinal and transversal samples were cut from the directionally solidified (DS) Al–8 wt%Ni ingot, for different positions from the cooled bottom to the top. The longitudinal sample was ground and etched with aqua regia solution (volume ratio of 3 HCl: 1  $\text{HNO}_3$ ) to reveal the macrostructure, while transversal samples were ground, polished and etched with 0.5% HF in water for 10–30 s to permit the microstructure to be examined. More details about the directional solidification process and the extraction of samples were described in a previous research [10].

The eutectic colony spacing ( $\lambda_{\text{EC}}$ ) and the secondary dendrite arm spacing ( $\lambda_2$ ) of the primary  $\text{Al}_3\text{Ni}$  phase were measured using the linear intercept method, for at least 50 measurements for each position along the length of the ingot. Employing the counting area method, the fibrous spacing ( $\lambda_{\text{F}}$ ) was measured at seven different positions. The alloy composition was analyzed from selected samples using a

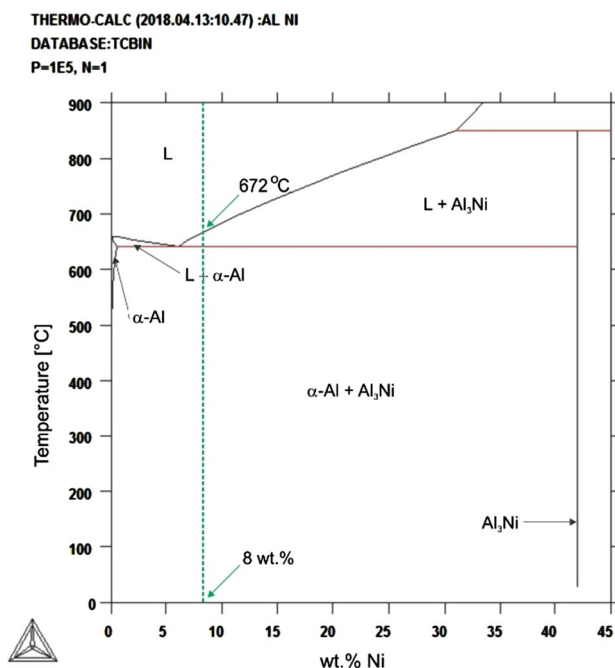


**Fig. 2** Partial Al–Ni binary phase diagram calculated by the Thermo-Calc software (database: TCBIN)

Panalytical X-Ray Fluorescence (XRF) spectrometer, model Axios. The present phases were determined by X-ray diffraction (XRD) technique with a Panalytical diffractometer, model X'pert PRO MRD XI, with Cu-K $\alpha$  and wavelength of 1.54 Å. The microstructure was analyzed through a Zeiss Evo-MA15 scanning electron microscopy (SEM) equipped with an Oxford X-Max energy-dispersive X-ray spectroscopy (EDS). Microhardness tests were performed using a Vickers tester FV-800 from Future-Tech, applying a test load of 0.5 kgf for 15 s, and adopting, at least, 20 measurements for each analyzed position. For comparison purposes, an Al–6.3 wt%Ni eutectic alloy was solidified in the same way, and similar samples were also subjected to Vickers microhardness tests.

### 3 Results and discussion

The macrostructure of the DS Al–8 wt%Ni alloy ingot is shown in Fig. 3, in which a columnar-to-equiaxed transition (CET) can be observed at about 32 mm from the cooled bottom. Some studies [16–18] report investigations on this transition that is of utmost importance in solidification processing since it affects the resulting properties of the as-solidified ingot. For example, equiaxed grains are preferred to be obtained in continuous casting processes leading to microstructural homogeneity [19], relevant for further metalworking. In contrast, columnar grains are more appropriate for polycrystalline turbine blades, with the grains oriented parallel to the principal stress axis of the blade [20]. Thermal gradient ( $G$ ) and growth rate ( $V$ ) ahead of the liquidus isotherm have been analyzed as solidification parameters influencing CET, but a critical value of the tip cooling rate, which encompasses both parameters ( $\dot{T}$ ), has been reported to be a more realistic criterion determining the macrostructural transition [21]. Concerning hypoeutectic Al–Ni alloys, the columnar growth was reported to prevail above a critical tip cooling rate of about 0.16 °C/s [22]. In the present investigation, it seems that the higher alloy Ni content and the different nature of solidification of the hypereutectic Al–8 wt%Ni alloy have induced the CET to occur at a higher  $\dot{T}$  of about 4.8 °C/s. The microstructure in the columnar region is characterized by eutectic colonies, while the equiaxed region has the  $\text{Al}_3\text{Ni}$  primary phase immersed in a eutectic matrix, which is typical of a hypereutectic microstructure, as shown in Fig. 3. It is worth noting that both the macrostructure and the microstructure of the alloy have been affected not only by a constitutional factor but also by the wide range of solidification cooling rates associated with the unsteady-state solidification regime of the present experimental study.

In contrast, when Al–Si hypereutectic alloys were solidified at the same unsteady-state conditions, under a range of

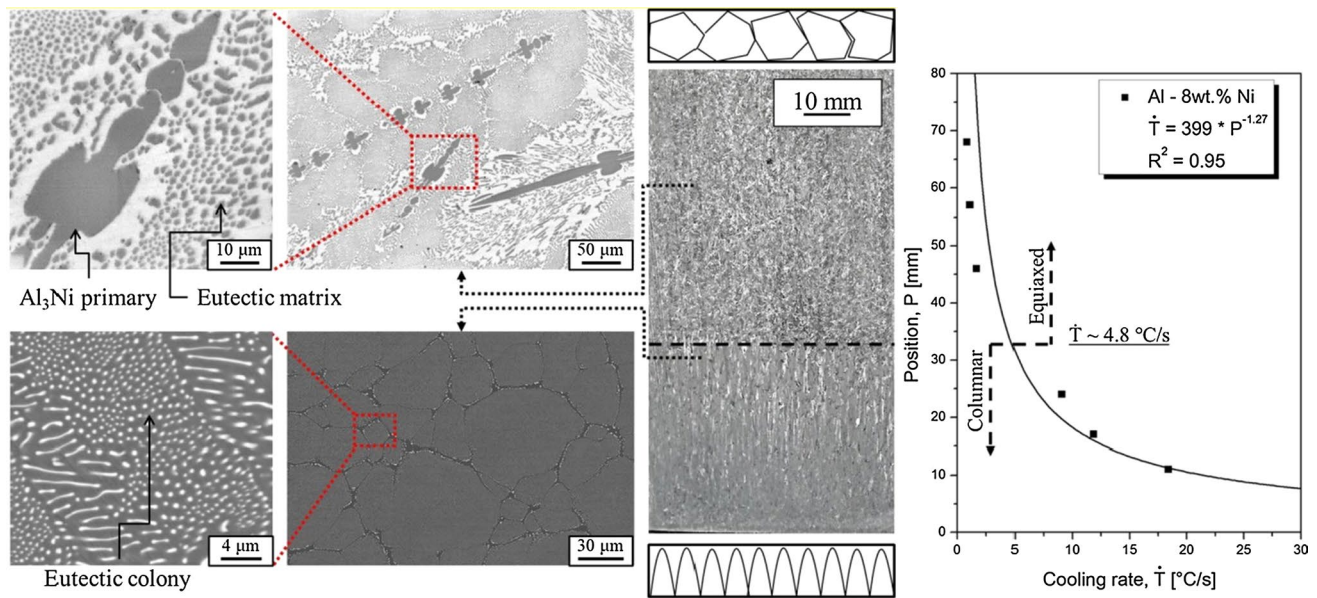


**Fig. 3** Macrostructure, SEM microstructure and evolution of the solidification cooling rate from the cooled bottom to the top of the Al-8 wt%Ni alloy ingot

cooling rates from 0.5 to 54 °C/s, CET was not observed [10]. However, as the microstructure was composed entirely of primary Si (with and without  $\alpha$ -Al dendritic halo) and eutectic, the primary phases may have blocked the growth of the columnar grains, thus permitting only equiaxed grains to prevail.

The  $\alpha$ -Al phase and the  $\text{Al}_3\text{Ni}$  IMC have been identified by XRD spectra, SEM images and EDS. X-ray diffraction patterns permitted the identification of the  $\alpha$ -Al and  $\text{Al}_3\text{Ni}$  phases all along the entire length of the DS ingot, as can be noticed for positions 10, 25 and 60 mm (Fig. 4). Figure 4b shows results from EDS analyzes, where the dark phase corresponds to the  $\alpha$ -Al phase as the compositions of points 1# and #6 represent a supersaturated Al solid solution with 0.23 at.%Ni. The maximum solubility of Ni in Al, under equilibrium conditions, is reported by Okamoto [23] to be 0.11 at.%Ni. The bright phase, points #4 and #7 (Fig. 4c, d), is  $\text{Al}_3\text{Ni}$  since the Ni content, about 24 at.% is in accordance with the one reported by Okamoto [23], that is 25 at.%. Fe is associated with Points #2 and #8 (Fig. 4b, d), since it is a common impurity in commercial grade Al, as mentioned in the Experimental Procedure section. It seems that the amount of Fe in the alloy ( $\sim 0.1$  wt%) has been rejected during the formation of both eutectic colonies and the primary phase and is located at the boundaries of the eutectic colonies. Moreover, a study in the literature reported that the  $\text{Al}_3\text{Ni}$  phase can dissolve up to 1 wt% of Fe [24]. Due to the reduced Fe content in the alloy, EDS elemental mapping was not able to show its distribution (Fig. 4). In the same

figure, Al and Ni are clearly shown in the  $\alpha$ -Al phase and in the  $\text{Al}_3\text{Ni}$  IMC. On the other hand, the solute concentration along the length of the Al-8 wt%Ni alloy ingot, determined by XRF (Fig. 5), shows the occurrence of a slight higher Ni concentration (9 wt%) at the position  $P=5$  mm. This is probably due to two factors: (1) the high cooling rates at this region, 30–50 K/s (Fig. 3), hindering diffusion of species; (2) low solubility of Ni in aluminum, as previously mentioned. In further positions the Ni concentrations are quite close to the nominal composition of the alloy along the length of the whole ingot, as well as for Fe.

Normally, a regular eutectic system has a symmetrical coupled zone (left side of Fig. 6); however, in the Al-Ni system the coupled zone is shifted toward the hypereutectic side, i.e. forming the mixture  $\alpha$ -Al- $\text{Al}_3\text{Ni}$  for high cooling rates (extending the range for which the eutectic microstructure occurs). The right side of Fig. 6 synthesizes some results of microstructural observation related to the alloy Ni content and solidification cooling rates, involving hypoeutectic, eutectic (5.7–6.3 wt%Ni) and hypereutectic Al-Ni alloys, to propose an asymmetric coupled zone diagram [4, 9, 25–28]. It is worth mentioning that to the best knowledge of the present authors, there is not any contribution in the literature concerning the analysis of microstructures of hypereutectic Al-Ni alloys related to a wide range of solidification cooling rates. Usually, the influence of the cooling rate on hypereutectic alloys is focused on the Al-Si system [10, 29, 30], due the inherent commercial interest of such alloys, but other alloys systems are gaining attention, e.g., Al-Co [31], Al-Cu

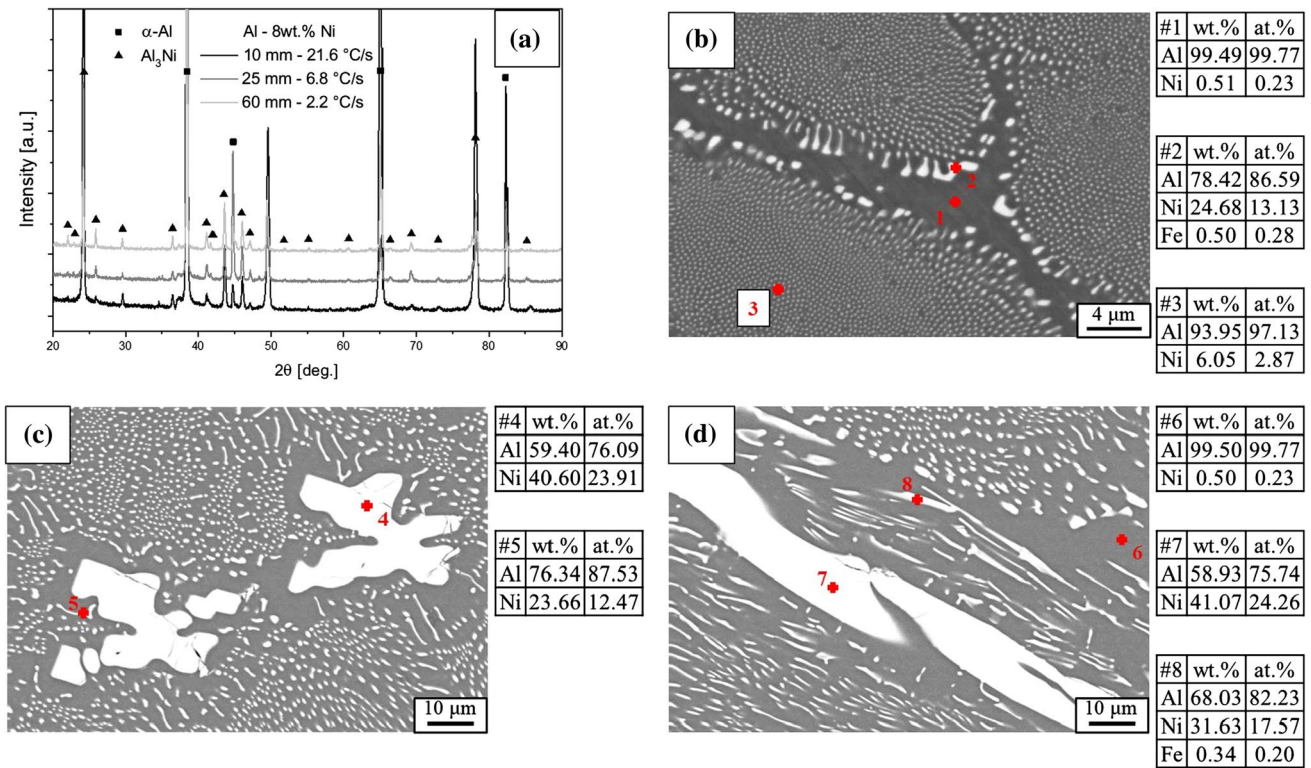
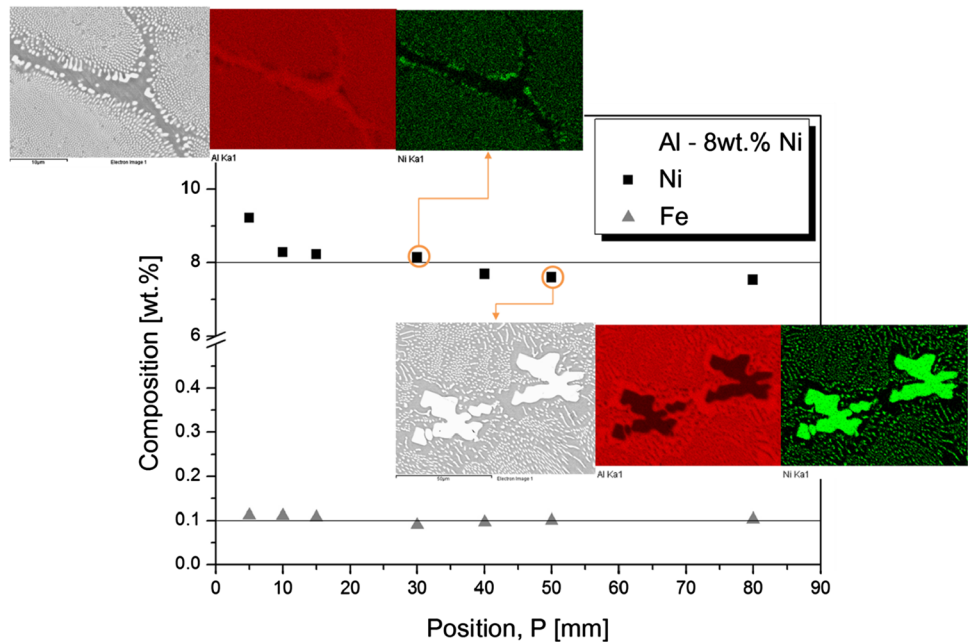


Fig. 4 Analyses of a XRD and SEM-EDS for samples from positions b 25 mm and c, d 60 mm along the length of the Al-8 wt%Ni alloy ingot

Fig. 5 Ni and Fe profiles along the length of the Al-8 wt%Ni alloy ingot



[32, 33] and Al-Sc [34], aiming the formation of metallic matrix composites.

According to the coupled zone theory [35–37], there is a competition between the growth of the primary phase and that of the eutectic mixture, which could be related to the undercooling. So, a fully eutectic microstructure could grow

during solidification of: (i) hypoeutectic and hypereutectic alloys at low cooling rates, associated with low undercooling; (ii) eutectic alloys in any condition; and (iii) hypereutectic alloys at high cooling rates. A very low undercooling is not capable to change the kinetics of the solidification front, in which a planar interface is maintained and the formation

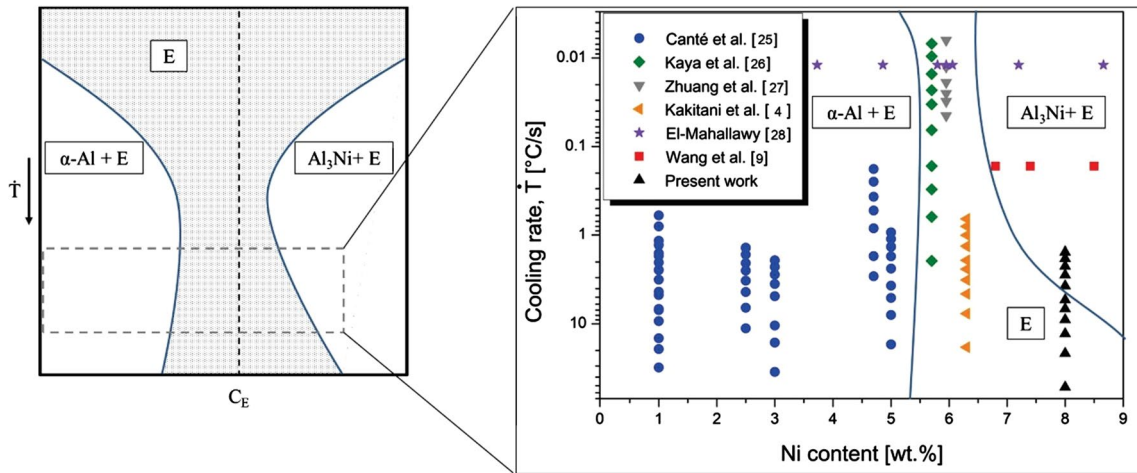


Fig. 6 Asymmetric coupled zone of the Al-8 wt%Ni alloy as a function of  $\dot{T}$ , where  $E$  is the eutectic

of primary phases in off-eutectic alloys is hindered. In the case of hypereutectic alloys, there is a limit of undercooling that favors the precipitation of primary  $Al_3Ni$ , and above this point, the instability due to the high cooling rate induces the formation of the eutectic phase, but with a non-planar interface. The difference in the eutectic growth is remarkable in the microstructure, where  $Al_3Ni$  fibers in the  $\alpha-Al$  matrix are found for low undercooling and eutectic colonies are present for high cooling rates. In addition, the absence of a fully eutectic mixture in hypoeutectic alloys for high cooling rates is related to the non-faceted growth of the  $\alpha-Al$  dendrites.

The evolutions of the interphase spacing, given by eutectic colony spacing ( $\lambda_{EC}$ ) and secondary arm spacing ( $\lambda_2$ ) as a function of  $\dot{T}$ , have been experimentally determined and are plotted in Fig. 7a. Figure 7a, b also schematically illustrates how  $\lambda_{EC}$ ,  $\lambda_2$  and  $\lambda_F$  have been measured. Experimental growth laws in the form of power functions relating  $\lambda_{EC}$  and  $\lambda_2$  to  $\dot{T}$  have been derived and set by specific power expressions with  $-1/4$  and  $-1/3$  exponents, for different range of cooling rates, that is  $\dot{T} > 4.8$  °C/s and  $\dot{T} < 4.8$  °C/s, respectively, due to the microstructural transition. The  $-1/4$  exponent is typical of the eutectic growth [38] while  $-1/3$  is generally associated with the growth of secondary arm spacings [39]. Figure 7b also shows the variation of the fibrous spacing ( $\lambda_F$ ) as a power function of  $\dot{T}$  with a  $-1/4$  exponent, although with different multipliers for each microstructural arrangement. It is worth mentioning that the region of eutectic colonies presented the same  $\lambda_F$  law reported for the growth of a eutectic Al-6.3 wt%Ni alloy [4]. For positions from the cooled surface toward the top of the DS Al-Ni ingot, i.e., with decreasing  $\dot{T}$ , all aforementioned microstructural spacings increase.

Figure 8 shows the results of Vickers microhardness (HV) measured along the length of the DS ingots against representative microstructural spacings,  $\lambda_C$ ,  $\lambda_2$  and  $\lambda_F$ . A

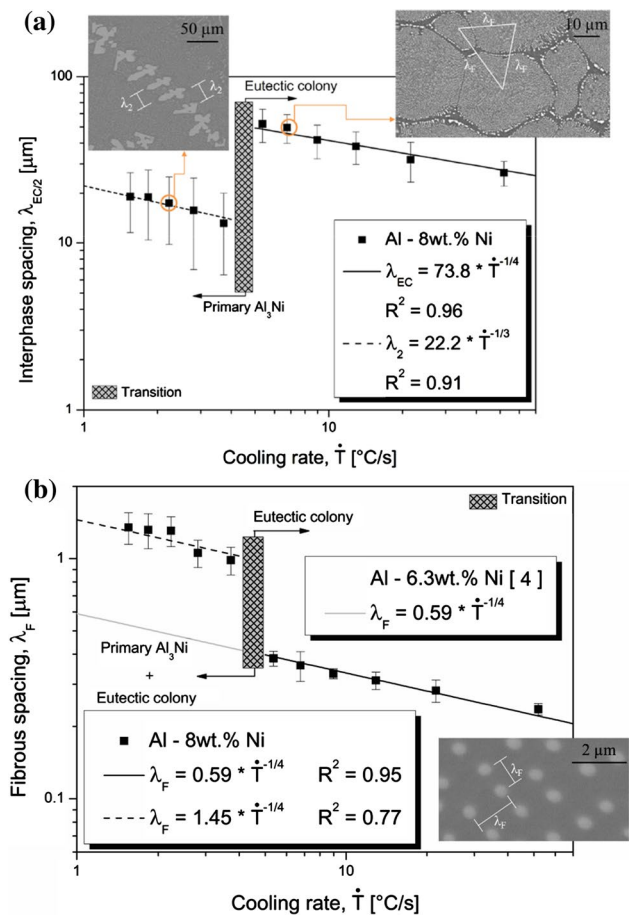
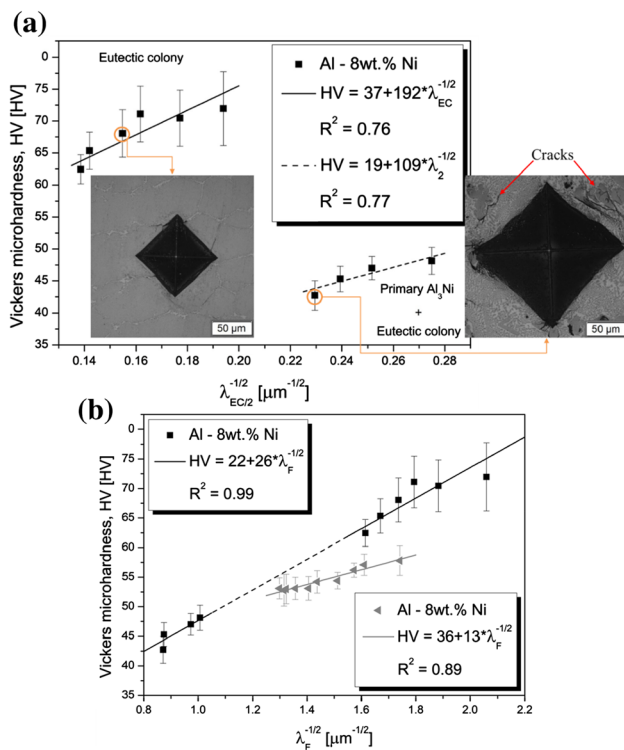


Fig. 7 Evolution of **a** interphase spacings (eutectic colony and secondary arm) and **b** fibrous spacings versus cooling rate along the length of the Al-8 wt%Ni alloy ingot.  $R^2$  is the coefficient of determination



**Fig. 8** Vickers microhardness as a function of **a**  $\lambda_{EC/2}^{-1/2}$  and **b**  $\lambda_F^{-1/2}$  along the length of the Al–8 wt%Ni alloy ingot.  $R^2$  is the coefficient of determination

Hall–Petch-type correlation is proposed relating HV to the microstructural spacings by a  $-1/2$  exponent. The Hall–Petch law was originally proposed to relate the yield strength to the grain size of a polycrystalline alloy. This law is based on the dislocation mechanisms of plastic deformation, particularly attributing the hindering effect of the grain boundaries to the movement of dislocations [40]. Since the interior of a grain is not uniform due to the existence of phases and intermetallics, the resistance to dislocation motion has also the significant contribution of these internal constituents of the grain. For this reason, Hall–Petch-type correlations relating tensile properties to the length scale of other characteristic microstructural features, such as interphase and dendritic arm spacings, have been recently proposed in the literature [26, 41, 42]. Since the imprint area caused by the hardness indentation testing is related to plastic deformation mechanisms, the hardness of metallic alloys has also been correlated with microstructural spacings by using Hall–Petch-type laws [43–46]. The region with presence of the  $Al_3Ni$  primary phase (Fig. 8a) presented a lower hardness profile than that of with eutectic colonies. The brittle behavior of the  $Al_3Ni$  primary phase can be realized by the cracks around the indentation mark (right side of Fig. 8a), which are responsible for the reduction in hardness. The brittle

shortcomings can be compensated by embedding fine  $Al_3Ni$  fibers homogeneously dispersed in the ductile  $\alpha$ -Al matrix, as such organized as eutectic colonies shown in the present study, favoring in this way the efficiency in the blockage of dislocations.

Figure 8b shows a unique HV correlation law when only  $\lambda_F$  is considered. The dotted line in the straight line represents a region without measurement, suppressed by the microstructural transition. The fineness of the microstructure, i.e., larger  $\lambda^{-1/2}$  values are responsible for the increase in hardness. Figure 8b also comparatively shows the correlation between hardness and  $\lambda_F$  for the eutectic Al–6.3 wt%Ni alloy. Concerning the eutectic colonies, both hypereutectic and eutectic alloys have the same morphology. So, the higher hardness profile provided by the hypereutectic alloy (Fig. 8b) seems to be related to the strengthening caused by the formation of a supersaturated solid solution of Ni in  $\alpha$ -Al. From the basic concept of metallurgy concerning solid solution, at which the addition of a metal to another provokes the increase in strength and hardness, an excess of Ni, which is present in solution of aluminum, is expected to generate stresses in the crystal lattice of aluminum, which contribute to hinder the movement of dislocations during plastic deformation [47]. Due to the high cooling rates associated with the non-equilibrium solidification conditions of the present study, the alloy solidifies and cools rapidly, thus permitting to retain as much as possible Ni in the  $\alpha$ -Al phase, which is considered an unstable condition where the solid solubility is exceeded at room temperature. Unsteady-state solidification could also have not only avoided the precipitation of the  $Al_3Ni$  primary phase at the first 32 mm of the ingot, but also favored Ni to be retained in  $\alpha$ -Al along the entire ingot by hindering diffusion, which is critical since the atomic radius of Ni is larger than that of Al [48], that is, an opposite situation as compared to that when smaller atoms diffuse more easily leading to precipitation.

Therefore, the benefits of high cooling rates in the solidification of Al–Ni alloys are the formation of eutectic colonies, decreasing the precipitation of primary  $Al_3Ni$  particles, and the solid solution supersaturation. In usual casting conditions, other Al–Ni hypereutectic alloys generally do not reach the same level of hardness, even with the addition of more Ni or other elements. Even though the addition of 2 wt% of Sc to an as-cast Al–10 wt%Ni alloy was reported to increase the hardness, due to the refinement of the microstructure and precipitation of new IMCs, such hardness was found to be lower than 55 HV [49]. In the study of Gonzales et al. [2], the as-cast Al–8.3 wt%Ni alloy was shown to have a hardness of 58 HV, while Chankitmongk et al., [50] found a hardness of about 44 HB for an as-cast Al–8 wt%Ni–0.3 wt%Zr alloy, which after aging treatment achieved a maximum hardness of about 53 HB.

## 4 Conclusions

The following conclusions can be drawn from the present experimental investigation:

- The macrostructure of the DS Al–8 wt%Ni alloy ingot is characterized by a columnar-to-equiaxed transition (CET) that occurred at a solidification cooling rate ( $\dot{T}$ ) of about 4.8 °C/s. The microstructure in the columnar region is formed by eutectic colonies, while the equiaxed region has the Al<sub>3</sub>Ni primary phase immersed in a eutectic matrix, which is typical of a hypereutectic microstructure.
- The observation of microstructures related to the alloy Ni content and solidification cooling rates, involving hypoeutectic, eutectic (5.7–6.3 wt%Ni) and hypereutectic Al–Ni alloys, has permitted an asymmetric coupled zone diagram (cooling rate versus alloy Ni content) to be proposed, in which the coupled zone is shifted toward the hypereutectic side of the diagram.
- The evolutions of the microstructural interphase spacings, given by eutectic colony spacing ( $\lambda_{EC}$ ) and secondary arm spacing ( $\lambda_2$ ), have been experimentally determined in the form of power functions relating  $\lambda_{EC}$  and  $\lambda_2$  to  $\dot{T}$ .
- The Vickers microhardness (HV) was shown to decrease with the increase in the microstructure length scale. A Hall–Petch-type correlation is proposed relating HV to the microstructural spacings by a  $-1/2$  exponent. A higher hardness profile was shown to be associated with the hypereutectic alloy as compared to that of a eutectic alloy. This seems to be related to the strengthening caused by the formation of a supersaturated solid solution of Ni in  $\alpha$ -Al.

**Acknowledgements** Brazilian Nanotechnology National Laboratory—LNNano, is gratefully acknowledged for the use of its facilities (XRD equipment).

**Funding** The authors are grateful to the National Council for Scientific and Technological Development (CNPq) and PIBIC/PRP-UNICAMP program for their financial support.

## Compliance with ethical standards

**Conflict of interest** The authors declare that there is no conflict of interest in this work.

## References

1. Poliarus O, Morgiel J, Umanskyi O, Pomorska M, Bodrowski P, Szczerba MJ, Kostenko O. Microstructure and wear of thermal sprayed composite NiAl-based coatings. *Archiv Civ Mech Eng*. 2019;19:1095–103.
2. Gonzalez G, Lara-Rodriguez GA, Sandoval-Jiménez A, Saikaly W, Charai A. The influence of cooling rate on the microstructure of an Al–Ni hypereutectic alloy. *Mater Charact*. 2008;59:1607–12.
3. Liu F, Zhu X, Ki S. Effects of Ni on the microstructure, hot tear and mechanical properties of Al–ZnMg–Cu alloys under as-cast condition. *J Alloys Compd*. 2020;821:153458.
4. Kakitani R, Reyes RV, Garcia A, Spinelli JE, Cheung N. Relationship between spacing of eutectic colonies and tensile properties of transient directionally solidified Al–Ni eutectic alloy. *J Alloys Compd*. 2018;733:59–68.
5. Fan Y, Makhlof MM. The effect of introducing the Al–Ni eutectic composition into Al–Zr–V alloys on microstructure and tensile properties. *Mater Sci Eng, A*. 2016;654:228–35.
6. Akopyan TK, Belov NA, Naumova EA, Letyagin NV. New in situ Al matrix composites based on Al–Ni–La eutectic. *Mater Lett*. 2019;245:110–3.
7. Suwanpreecha C, Pandee P, Patakham U, Limmaneevichitr C. New generation of eutectic Al–Ni casting alloys for elevated temperature services. *Mater Sci Eng, A*. 2018;709:46–54.
8. Fan Y, Huang K, Makhlof MM. Precipitation strengthening in Al–Ni–Mn alloys. *Metall Mater Trans A*. 2015;46:5830–41.
9. Wang Q, Wang ZY, Liu T, Wang CJ, Zhang C, He JC. Alignment of primary Al<sub>3</sub>Ni phases in hypereutectic Al–Ni alloys with various compositions under high magnetic fields. *Sci China Ser E*. 2009;52:857–63.
10. Reyes RV, Bello TS, Kakitani R, Costa TA, Garcia A, Cheung N, Spinelli JE. Tensile properties and related microstructural aspects of hypereutectic Al–Si alloys directionally solidified under different melt superheats and transient heat flow conditions. *Mater Sci Eng, A*. 2017;685:235–43.
11. Feng H, Yang Z, Bai Y, Zhang L, Liu Y. Effect of Cr content and cooling rate on the primary phase of Al–2.5Mn alloy. *Int J Miner Metall Mater*. 2019;26:1551–8.
12. Ourfali MF, Todd I, Jones H. Effect of solidification cooling rate on the morphology and number per unit volume of primary Mg<sub>2</sub>Si particles in a hypereutectic Al–Mg–Si alloy. *Metall Mater Trans A*. 2005;36:1368–72.
13. Zuo KS, Zhang HT, Han X, Jia HL, Qin K, Cui JZ. Effects of Cr and cooling rate on segregation and refinement of primary Si in Al–20 wt%Si alloy. *Int Metalcast*. 2014;8:55–62.
14. Kakitani R, Reyes RV, Garcia A, Cheung N, Spinelli JE. Effects of melt superheating on the microstructure and tensile properties of a ternary Al–15 Wt Pct Si–1.5 Wt Pct Mg alloy. *Metall Mater Trans A*. 2019;50:1308–22.
15. Dias M, Oliveira R, Kakitani R, Cheung N, Henein H, Spinelli JE, Garcia A. Effects of solidification thermal parameters and Bi doping on silicon size, morphology and mechanical properties of Al–15wt% 3.2wt% Bi and Al–18wt% 3.2wt% Bi alloys. *J Mater Res Technol*. 2020;9:3460–70.
16. Lekakh SN, O’Malley R, Emmendorfer M, Hrebec B. Control of columnar to equiaxed transition in solidification macrostructure of austenitic stainless steel castings. *ISIJ Int*. 2017;57:824–32.
17. Leriche N, Combeau H, Gandin C-A, Založnik M. Modelling of columnar-to-equiaxed and equiaxed-to-columnar transitions in ingots using a multiphase model. *IOP Conf Ser-Mat Sc*. 2015;84:012087.
18. Svidró P, Diószegi A. Determination of the columnar to equiaxed transition in hypoeutectic lamellar cast iron. *ISIJ Int*. 2014;54:460–5.



19. Wang H, Zhao P, Chen J, Li M, Yang Z, Wu C. Original position statistic distribution analysis study of low alloy steel continuous casting billet. *Sci China Ser E*. 2005;48:104–15.
20. Bhaumik SK, Bhaskaran TA, Rangaraju R, Venkataswamy MA, Parameswara MA, Krishnan RV. Failure of turbine rotor blisk of an aircraft engine. *Eng Fail Anal*. 2002;9:287–301.
21. Siqueira CA, Cheung N, Garcia A. Solidification thermal parameters affecting the columnar-to-equiaxed transition. *Metall Mater Trans A*. 2002;33:2107–18.
22. Canté MV, Cruz KS, Spinelli JE, Cheung N, Garcia A. Experimental analysis of the columnar-to-equiaxed transition in directionally solidified Al–Ni and Al–Sn alloys. *Mater Lett*. 2007;61:2135–8.
23. Okamoto H. Al–Ni (Aluminum–Nickel). *J Phase Equilib*. 1993;14:257–9.
24. Glazoff MV, Khvan A, Zolotarevsky VS, Belov NA, Dinsdale A. Casting aluminum alloys: their physical and mechanical metallurgy. Oxford: Butterworth-Heinemann; 2018.
25. Canté MV, Spinelli JE, Cheung N, Garcia A. The correlation between dendritic microstructure and mechanical properties of directionally solidified hypoeutectic Al–Ni alloys. *Met Mater Int*. 2010;16:39–49.
26. Kaya H, Böyük U, Çadırılı E, Maraşlı N. Measurements of the microhardness, electrical and thermal properties of the Al–Ni eutectic alloy. *Mater Des*. 2012;34:707–12.
27. Zhuang YX, Zhang XM, Zhu LH, Hu ZQ. Eutectic spacing and faults of directionally solidified Al–Al<sub>3</sub>Ni eutectic. *Sci Technol Adv Mater*. 2001;2:37–9.
28. El-Mahallawy NA. Effect of composition on the structure of directionally solidified Al–Ni and Al–Ni–Cu composites. *Fibre Sci Technol*. 1983;19:27–36.
29. Yamagat H, Kasprzak W, Aniolek M, Kurita H, Sokolowski JH. The effect of average cooling rates on the microstructure of the Al–20% Si high pressure die casting alloy used for monolithic cylinder blocks. *J Mater Process Technol*. 2008;203:333–41.
30. Pierantoni M, Gremaud M, Magnin P, Stoll D, Kurz W. The coupled zone of rapidly solidified Al–Si alloys in laser treatment. *Acta Metall Mater*. 1992;40:1637–44.
31. Silva CAP, Kakitani R, Canté MV, Brito C, Garcia A, Spinelli JE, Cheung N. Microstructure, phase morphology, eutectic coupled zone and hardness of Al–Co alloys. *Mater Charact*. 2020;169:110617.
32. Li C, Yang H, Ren Z, Ren W, Wu Y. Application of differential thermal analysis to investigation of magnetic field effect on solidification of Al–Cu hypereutectic alloy. *J Alloys Compd*. 2010;505:108–12.
33. Li SM, Quan QR, Li XL, Fu HZ. Increasing the growth velocity of coupled eutectics in directional solidification of off-eutectic alloys. *J Cryst Growth*. 2011;314:279–84.
34. Jiang A, Wang X. Dendritic and seaweed growth of proeutectic scandium tri-aluminide in hypereutectic Al–Sc undercooled melt. *Acta Mater*. 2020;200:56–65.
35. Stefanescu DM. Science and engineering of casting solidification. 2nd ed. New York: Springer; 2009.
36. Li Y. Bulk metallic glasses: eutectic coupled zone and amorphous formation. *JOM*. 2005;57:60–3.
37. Kurz W, Fisher DJ. Dendrite growth in eutectic alloys: the coupled zone. *Int Met Rev*. 1979;24:177–204.
38. Garcia A, Prates M. Mathematical model for the unidirectional solidification of metals: I. cooled molds. *Metall Trans B*. 1978;9:449–57.
39. Spinelli JE, Cheung N, Garcia A. On array models theoretical predictions versus measurements for the growth of cells and dendrites in the transient solidification of binary alloys. *Philos Mag*. 2011;91:1705–23.
40. Hall EO. The deformation and ageing of mild steel: III discussion of results. *Proc Phys Soc*. 1951;64:747–53.
41. Vida TA, Brito C, Lima TS, Spinelli JE, Cheung N, Garcia A. Near-eutectic Zn–Mg alloys: interrelations of solidification thermal parameters, microstructure length scale and tensile/corrosion properties. *Curr Appl Phys*. 2019;19:582–98.
42. Gouveia GL, Kakitani R, Gomes LF, Afonso CRM, Cheung N, Spinelli JE. Slow and rapid cooling of Al–Cu–Si ultrafine eutectic composites: interplay of cooling rate and microstructure in mechanical properties. *J Mater Res*. 2019;34:1381–94.
43. Taha AS, Hammad FH. Application of the Hall–Petch relation to microhardness measurements on Al, Cu, Al–MD 105, and Al–Cu alloys. *Phys Status Solidi A*. 1990;119:455–62.
44. Brito C, Costa TA, Vida TA, Bertelli F, Cheung N, Spinelli JE, Garcia A. Characterization of dendritic microstructure, intermetallic phases, and hardness of directionally solidified Al–Mg and Al–Mg–Si alloys. *Metall Mater Trans A*. 2015;46:3342–55.
45. Bertelli F, Brito C, Ferreira IL, Reinhart G, Nguyen-Thi H, Mangelinck-Noël N, Cheung N, Garcia A. Cooling thermal parameters, microstructure, segregation and hardness in directionally solidified Al–Sn–(Si;Cu) alloys. *Mater Des*. 2015;72:31–42.
46. Verissimo NC, Brito C, Santos WLR, Cheung N, Spinelli JE, Garcia A. Interconnection of Zn content, macrosegregation, dendritic growth, nature of intermetallics and hardness in directionally solidified Mg–Zn alloys. *J Alloys Compd*. 2016;662:1–10.
47. Callister WD. Materials science and engineering: an introduction. 10th ed. Hoboken: Wiley; 2018.
48. MatWeb: Online materials information resource. 2019. <http://www.matweb.com/>. Accessed 15 Nov 2019.
49. Kilicaslan MF, Karakose E. Depth sensing indentation analyses of hypereutectic Al–10Ni–XSc (X = 0, 1, 2) alloys. *Met Mat Int*. 2017;23:473–80.
50. Chankitmongkol S, Eskin DG, Limmaneevichitr C. Structure refinement, mechanical properties and feasibility of deformation of hypereutectic Al–Fe–Zr and Al–Ni–Zr alloys subjected to ultrasonic melt processing. *Mater Sci Eng, A*. 2020;788:139567.

**Publisher's Note** Springer Nature remains neutral with regard to jurisdictional claims in published maps and institutional affiliations.